Check for updates

Evolutionary Aeroelastic Design of Flying-Wing Cross Section

Mojtaba Moshtaghzadeh[*] and Ehsan Izadpanahi[†]
Florida International University, Miami, Florida 33174
Adrian Bejan[‡]
Duke University, Durham, North Carolina 27708-0300
and
Pezhman Mardanpour[§]
Florida International University, Miami, Florida 33174

https://doi.org/10.2514/1.J060410

The uniform distribution of stresses in flying-wing aircraft improves the aeroelastic flight envelope. In this paper, we document the effect of wing cross-section configuration on the stress distribution and flutter characteristics of a flying-wing aircraft. We determined the flow of stresses through the wing structure, and changed the structure to avoid stress strangulations. The emerging structure is more stable. We used the computer programs Gmsh, Variational Asymptotic Beam Sectional Analysis, and Nonlinear Aeroelastic Trim and Stability of High Altitude Long Endurance Aircraft. The wing structure was evolved by holding fixed the flight condition, mass per unit length, and material type. The results indicate that particular configurations of wing cross sections favor a uniform stress distribution, and therefore aeroelastic stability. The configuration with higher flutter speed is associated with the smoother flow of stresses through the wing structure.

Downloaded by Karina Bustillo on September 13, 2021 | http://arc.aiaa.org | DOI: 10.2514/1.J060410

Nomenclature

a	=	deformed beam aerodynamic frame of reference
B	=	deformed beam cross-sectional frame of reference
b	=	undeformed beam cross-sectional frame of reference
$\boldsymbol{B}_i$	=	unit vectors of deformed beam cross-sectional frame of reference ($i = 1, 2, 3$)
$\boldsymbol{b}_i$	=	unit vectors in undeformed beam cross-sectional frame of reference ($i = 1, 2, 3$)
c	=	chord
C^{Bi}	=	transformation matrix from the inertial frame i to deformed frame B
C^{bi}	=	transformation matrix from the inertial frame i to deformed frame b
C^{iB}	=	transformation matrix from the deformed frame B to inertial frame i
C^{ib}	=	transformation matrix from the undeformed frame b to inertial frame i
c_{d_0}, c_{l_0}	=	aerodynamic drag and lift coefficients at zero angle of attack
$c_{l\alpha}$	=	lift coefficient with respect to (w.r.t.) angle of attack (α)
$c_{l\beta}$	=	lift coefficient w.r.t. flap deflection (β)
$c_{m\beta}$	=	pitch moment coefficient flap deflection (β)
e	=	offset of aerodynamic center from the origin of frame of reference along $\boldsymbol{b}_2$
e_1	=	column matrix
F	=	column matrix of internal force measured in $\boldsymbol{B}_i$ basis
f	=	column matrix of distributed, applied force measured in $\boldsymbol{B}_i$ basis
$\boldsymbol{g}$	=	gravitational vector in $\boldsymbol{B}_i$ basis
H	=	column matrix of cross-sectional angular momentum measured in $\boldsymbol{B}_i$ basis
I	=	cross-sectional inertia matrix
i	=	inertial frame of reference
$\boldsymbol{i}_i$	=	unit vectors for inertial frame of reference, where i is equal to 1, 2, 3
K	=	column matrix of deformed beam curvature and twist measured in $\boldsymbol{B}_i$ basis
k	=	column matrix of undeformed beam initial curvature and twist measured in $\boldsymbol{b}_i$ basis
M	=	column matrix of internal moment measured in $\boldsymbol{B}_i$ basis
m	=	column matrix of distributed, applied moment measured in $\boldsymbol{B}_i$ basis
P	=	column matrix of cross-sectional linear momentum measured in $\boldsymbol{B}_i$ basis
r	=	column matrix of position vector measured in $\boldsymbol{b}_i$ basis
u	=	column matrix of displacement vector measured in $\boldsymbol{b}_i$ basis
V	=	column matrix of velocity measured in $\boldsymbol{B}_i$ basis
x_1	=	axial coordinate of beam
α	=	angle of attack
β	=	trailing-edge flap angle
γ	=	column matrix of one-dimensional (1-D) generalized force strain measures
Δ	=	identity matrix
κ	=	column matrix of elastic twist and curvature measures (1-D generalized moment strain measures)
λ	=	column matrix of induced flow states
μ	=	mass per unit length
ξ	=	column matrix of center of mass offset from the frame-of-reference origin
ρ	=	air density
ψ	=	column matrix of small incremental rotations
Ω	=	column matrix of cross-sectional angular velocity
$()'$	=	partial derivative with respect to x_1
$\dot{()}$	=	partial derivative with respect to time
$\hat{()}$	=	nodal variable

Received 2 December 2020; revision received 1 July 2021; accepted for publication 7 July 2021; published online 7 September 2021. Copyright © 2021 by Mojtaba Moshtaghzadeh, Ehsan Izadpanahi, Adrian Bejan, and Pezhman Mardanpour. Published by the American Institute of Aeronautics and Astronautics, Inc., with permission. All requests for copying and permission to reprint should be submitted to CCC at www.copyright.com; employ the eISSN 1533-385X to initiate your request. See also AIAA Rights and Permissions www.aiaa.org/randp.

*Graduate Research Assistant, Department of Mechanical and Material Engineering; mmosh009@fiu.edu.

†Postdoctoral Associate, Department of Mechanical and Material Engineering; eizad001@fiu.edu.

‡Professor, Department of Mechanical Engineering and Materials Science; abejan@duke.edu.

§Assistant Professor, Department of Mechanical and Material Engineering; Pezhman.Mardanpour@fiu.edu. Member AIAA.

I. Introduction

NEW ideas guide the design of new aircraft that can fly faster and farther, and consume less fuel. To this end, helpful is a design theory that can predict the evolutionary trend in the design and performance of aircraft. The *constructal law* is the basis for such a

Downloaded by Karina Bustillo on September 13, 2021 | http://arc.aiaa.org | DOI: 10.2514/1.J060410

theory [1–6]. It is the law of physics that accounts for the phenomenon of evolution in nature: "For a finite-size flow system to persist in time (to live), its configuration must evolve freely such that it provides greater access to its currents."

Constructal law governs energy flow configuration and evolutionary design in nature [7,8]. Many constructal law applications to the evolutionary design of engineering and biological systems are reviewed in articles and books [7–9]. Constructal law anticipates the evolution of airplanes, helicopters, and ships that are in complete accord with the evolution of animal locomotion [1–4]. The constructal approach predicts the evolution of the most basic physical characteristics, such as fuel load, speed, wingspan, fuselage, length, and engine size [1,3,5]. Large or small, airplanes exhibit a proportionality between wingspan and fuselage length, and between fuel load and body size [1,6]. This scaling is analogous to animal design, where the mass of the motive organs (muscles, heart, lungs) is proportional to the body size [1].

Optimization methods have been used frequently in the design of aircraft parts. Rao et al. [10] employed a topology optimization method to develop an optimal aircraft wing. They selected the isotruss construction for the Dornier aircraft wing. They found an optimal design as well as the optimum shape and material distribution, which are subjected to a specific set of constraints. Schuhmacher et al. [11] used the multidisciplinary design optimization method to design a wing box for a Fairchild Dornier regional jet. The topology optimization was used by Zhu et al. [12] to investigate dynamic responses, aircraft body structure, and shape-preserving design in aerospace systems. Oktay et al. [13] determined the optimum design of the ribs by using topology optimization and computational fluid dynamics. Most of the studies of the aircraft wing considered the wing as a thin-wall beam structure [14–19].

In the present study, we use the constructal law and the evolution of the flow of stresses to design different wing rib configurations, including rectangular, triangle, polygon, circle, and oval. The concept of flow of stresses was introduced in evolutionary design by Bejan and coworkers [8,20,21], who showed that if the strangulation of internal stresses are avoided, the loaded structure is the lightest and strongest.

Mardanpour et al. [6] presented the effect of engine placement on the aeroelastic stability and flow of stress through the aircraft wing. They showed that there is a relationship between aeroelastic instability and stress strangulation. Their study simulated the engines of a flying wing as rigid bodies with thrusts, angular momentums, masses, and inertias. These engines represented discontinuities in terms of externally applied loads. Their results showed that these discontinuities' locations significantly affect the flow of stresses, hence the aeroelastic flight envelope.

Furthermore, Izadpanahi et al. [22] showed that the curvature and sweep of the wing can affect the aeroelastic stability and stress distribution of flying-wing aircraft. They found that higher flutter speed could be achieved if strangulation is avoided in the flow of stresses.

The wing contains a frame that is constructed from spars, ribs, and stringers. Ribs play a vital role in carrying the air load from the wing surface to the spars [23]. In this paper, we explore the effect of wing ribs on the stability and flow of stresses of a flying-wing aircraft. We seek a better cross-section configuration that has a smoother flow of stresses and higher stability. Aircraft with nine different wing cross-section configurations are designed, and the stability analyses are performed to obtain the flutter characteristic. Next, we trim the aircraft under the same cruise condition, and we present the stresses in several directions to document the flow of stresses through a flying aircraft wing.

II. Theory

The structure of a wing-shaped body loaded in bending was studied as an evolutionary design for stresses and fluid flow in Kim et al. [24] and Ref. [8] (section 8.6 and problem 8.1). In the following work, the wing is treated as an elastic body subjected to three-dimensional time-dependent aerodynamic loading, whereas the design of the structure evolves toward smoother flow of stresses and higher flutter speed.

A. Nonlinear Composite Beam Theory

The fully intrinsic nonlinear composite beam theory is based on first-order partial differential equations of motion for the beam, which are independent of displacement and rotation variables. The equations contain variables that are expressed in terms of the bases of the reference frames for the undeformed and deformed beams, $b(x_1)$ and $B(x_1, t)$, respectively; see Fig. 1. These equations are based on force, moment, angular velocity, and velocity with nonlinearities of second order. The equations of motion are

$$\begin{aligned} F_B' + \tilde{K}_B F_B + f_B &= \dot{P}_B + \tilde{\Omega}_B P_B \\ M_B' + \tilde{K}_B M_B + (\tilde{e}_1 + \tilde{\gamma}) F_B + m_B &= \dot{H}_B + \tilde{\Omega}_B H_B + \tilde{V}_B P_B \end{aligned} \tag{1}$$

where the generalized strains and velocities are related to stress resultants and moments by the structural constitutive equations

$$\begin{Bmatrix} \gamma \\ \kappa \end{Bmatrix} = \begin{bmatrix} R & S \\ S^T & T \end{bmatrix} \begin{Bmatrix} F_B \\ M_B \end{Bmatrix} \tag{2}$$

and the inertial constitutive equations [6]

$$\begin{Bmatrix} P_B \\ H_B \end{Bmatrix} = \begin{bmatrix} \mu\Delta & -\mu\tilde{\xi} \\ \mu\tilde{\xi} & I \end{bmatrix} \begin{Bmatrix} V_B \\ \Omega_B \end{Bmatrix} \tag{3}$$

Finally, strain- and velocity-displacement equations are used to derive the intrinsic kinematical partial differential equations [25], which are given as [6]

$$\begin{aligned} V_B' + \tilde{K}_B V_B + (\tilde{e}_1 + \tilde{\gamma}) \Omega_B &= \dot{\gamma} \\ \Omega_B' + \tilde{K}_B \Omega_B &= \dot{\kappa} \end{aligned} \tag{4}$$

In this set of equations, F_B and M_B are column matrices of cross-sectional stress and moment resultant measures in the B frame, respectively; V_B and Ω_B are column matrices of cross-sectional frame velocity and angular velocity measures in the B frame, respectively; P_B and H_B are column matrices of cross-sectional linear and angular momentum measures in the B frame, respectively; R, S, and T are 3×3 partitions of the cross-sectional flexibility matrix; Δ is the 3×3 identity matrix; I is the 3×3 cross-sectional inertia matrix; ξ is $\lfloor 0 \quad \xi_2 \quad \xi_3 \rfloor^T$, with ξ_2 and ξ_3 representing the position coordinates of the cross-sectional mass center with respect to the reference line; μ is the mass per unit length; $\tilde{()}$ denotes the antisymmetric 3×3 matrix associated with the column matrix over which the tilde is placed; $\dot{()}$ denotes the partial derivative with respect to time; and $()'$ denotes the partial derivative with respect to the axial coordinate, x_1. More details

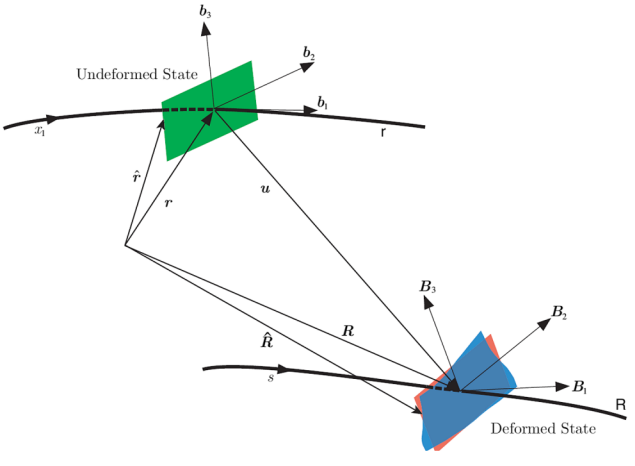

Fig. 1 Schematic of beam deformation [25].

about these equations can be found in Ref. [26]. This is a complete set of first-order, partial differential equations. To solve the system of equations, one may eliminate γ and κ using Eq. (3) and P_B and H_B using Eq. (4). Then, 12 boundary conditions are needed in terms of force F_B, moment M_B, velocity V_B, and angular velocity Ω_B. The maximum degree of nonlinearities is two, and because displacement and rotation variables do not appear, singularities caused by finite rotations are avoided. If needed, the position and the orientation can be calculated as postprocessing operations by integrating

$$\begin{aligned} r_i' &= C^{ib} e_1 \\ r_i + u_i' &= C^{iB}(e_1 + \gamma) \end{aligned} \tag{5}$$

and

$$\begin{aligned} (C^{bi})' &= -\tilde{k} C^{bi} \\ (C^{Bi})' &= -(\tilde{k} + \tilde{\kappa}) C^{Bi} \end{aligned} \tag{6}$$

Here, C defines the transformation matrix, r is column matrix of position vector measured in $\boldsymbol{b}_i$ basis, and u indicates the column matrix of displacement vector measured in $\boldsymbol{b}_i$ basis [6].

B. Variational Asymptotic Beam Sectional Analysis (VABS)

Reference [27] adopted the variational asymptotic method (VAM) of Berdichevskii [28] to reduce the formulation of a three-dimensional elasticity problem into a one-dimensional (1-D) formulation. VAM finds the stationary point of a function that has one or more small parameters. It is the right tool for the dimensional reduction in structures such as beams, plates, and shells. This mathematical approach and the Hamilton extended principle lead to the geometrically exact nonlinear composite beam theory of Hodges and its cross-sectional analysis [26,27].

For the cross-sectional analysis, the solution to the minimization problem of VAM is obtained from a finite-element numerical approach that is built into the software package VABS. The results lead to the components of the 6×6 sectional constitutive and inertial matrices next [6]:

$$\begin{Bmatrix} \gamma_{11} \\ 2\gamma_{12} \\ 2\gamma_{13} \\ \kappa_1 \\ \kappa_2 \\ \kappa_3 \end{Bmatrix} = \begin{bmatrix} R_{11} & R_{12} & R_{13} & S_{11} & S_{12} & S_{13} \\ R_{12} & R_{22} & R_{23} & S_{21} & S_{22} & S_{23} \\ R_{13} & R_{23} & R_{33} & S_{31} & S_{32} & S_{33} \\ S_{11} & S_{21} & S_{31} & T_{11} & T_{12} & T_{13} \\ S_{12} & S_{22} & S_{32} & T_{12} & T_{22} & T_{23} \\ S_{13} & S_{23} & S_{33} & T_{13} & T_{23} & T_{33} \end{bmatrix} \begin{Bmatrix} F_1 \\ F_2 \\ F_3 \\ M_1 \\ M_2 \\ M_3 \end{Bmatrix} \tag{7}$$

$$\begin{Bmatrix} P_1 \\ P_2 \\ P_3 \\ H_1 \\ H_2 \\ H_3 \end{Bmatrix} = \begin{bmatrix} \mu & 0 & 0 & 0 & \mu\bar{x}_3 & -\mu\bar{x}_2 \\ 0 & \mu & 0 & -\mu\bar{x}_3 & 0 & 0 \\ 0 & 0 & \mu & \mu\bar{x}_2 & 0 & 0 \\ 0 & -\mu\bar{x}_3 & \mu\bar{x}_2 & i_2 + i_3 & 0 & 0 \\ \mu\bar{x}_3 & 0 & 0 & 0 & i_2 & i_{23} \\ -\mu\bar{x}_2 & 0 & 0 & 0 & i_{23} & i_3 \end{bmatrix} \begin{Bmatrix} F_1 \\ F_2 \\ F_3 \\ M_1 \\ M_2 \\ M_3 \end{Bmatrix} \tag{8}$$

VABS [27,29,30] is a commercial software that uses the variational method to simplify a three dimensional (3-D) nonlinear analysis. It projects 3-D slender structures to a two-dimensional (2-D) cross-sectional and one-dimensional (1-D) beam analysis. VABS decreases the analysis time from hours to seconds while maintaining the accuracy of detailed 3-D finite element analysis. It uses a finite element mesh of the cross section and material properties as inputs to calculate the cross-sectional properties (e.g., structural properties and inertial properties). It also performs stress recovery using inputs such as axial and shear forces, moments, distributed forces, and moments including applied and inertial [22].

C. Finite State Induced Model

The 2-D finite state aerodynamic model of Peters et al. [31] is a state-space, thin-airfoil, inviscid, incompressible approximation of an infinite-state representation of the aerodynamic loads, which accounts for induced flow in the wake and apparent mass effects, using known airfoil parameters. It accommodates large motion of the airfoil as well as deflection of a small trailing-edge flap. Although the two-dimensional version of this model does not account for three-dimensional effects associated with the wing tip, published data [31–33] show that this theory is an excellent approximation of aerodynamic loads acting on high-aspect-ratio wings. The lift, drag, and pitching moment at the quarter-chord are given by

$$\begin{aligned} L_{\text{aero}} = \rho b \Big[& (c_{l_0} + c_{l_\beta}\beta) V_T V_{a_2} - c_{l_\alpha} \dot{V}_{a_3} b/2 \\ & - c_{l_\alpha} V_{a_2} (V_{a_3} + \lambda_0 - \Omega_{a_1} b/2) - c_{d_o} V_T V_{a_3} \Big] \end{aligned} \tag{9}$$

$$D_{\text{aero}} = \rho b \Big[-(c_{l_0} + c_{l_\beta}\beta) V_T V_{a_3} + c_{l_\alpha} (V_{a_3} + \lambda_0)^2 - c_{d_o} V_T V_{a_2} \Big] \tag{10}$$

$$\begin{aligned} M_{\text{aero}} = 2\rho b \Big[& (c_{m_0} + c_{m_\beta}\beta) V_T - c_{m_\alpha} V_T V_{a_3} - b c_{l_\alpha}/8 V_{a_2} \Omega_{a_1} \\ & - b^2 c_{l_\alpha} \dot{\Omega}_{a_1}/32 + b c_{l_\alpha} \dot{V}_{a_3}/8 \Big] \end{aligned} \tag{11}$$

$$V_T = (V_{a_2}^2 + V_{a_3}^2)^{1/2} \tag{12}$$

$$\sin\alpha = \frac{-V_{a_3}}{V_T} \tag{13}$$

$$\alpha_{\text{rot}} = \frac{\Omega_{a_1} b/2}{V_T} \tag{14}$$

and V_{a_2}, V_{a_3} are the measured values of V_a, and β is the angle of flap deflection. The effect of unsteady wake (induced flow) and apparent mass appear as λ_0 and acceleration terms in the force and moment equations. The induced flow model of Peters et al. [31] is included to calculate λ_0 as

$$\left[A_{\text{induced flow}}\right]\{\dot{\lambda}\} + \left(\frac{V_T}{b}\right)\{\lambda\} = \left(-\dot{V}_{a_3} + \frac{b}{2}\dot{\Omega}_{a_1}\right)\left\{c_{\text{induced flow}}\right\} \tag{15}$$

$$\lambda_0 = \frac{1}{2}\left\{b_{\text{induced flow}}\right\}^T \{\lambda\} \tag{16}$$

where λ is the column matrix of induced flow states, and $[A_{\text{induced flow}}]$, $\{c_{\text{induced flow}}\}$, $\{b_{\text{induced flow}}\}$ are constant matrices derived in Refs. [6,31].

D. Aeroelastic System

The aeroelastic system is described by coupling the aerodynamic equations with the structural equations,

$$[A]\{\dot{x}\} + \{B(x)\} = \{f_{\text{cont}}\} \tag{17}$$

where, $\{x\}$ and f_{cont} represent the vector of all the aeroelastic variables and the vector of the flight controls, respectively. The resulting nonlinear ordinary differential equations are linearized about a static equilibrium state. The linearized system can be represented as

$$[A]\{\dot{\hat{x}}\} + [B]\{\hat{x}\} = \{\hat{f}_{\text{cont}}\} \tag{18}$$

where ($\hat{}$) indicates the perturbation about the steady-state values [6].

The equilibrium state is governed by nonlinear algebraic equations, which the code Nonlinear Aeroelastic Trim and Stability of HALE Aircraft (NATASHA) [34,35] solves to obtain the steady-state

Downloaded by Karina Bustillo on September 13, 2021 | http://arc.aiaa.org | DOI: 10.2514/1.J060410

Downloaded by Karina Bustillo on September 13, 2021 | http://arc.aiaa.org | DOI: 10.2514/1.J060410

trim solution using the Newton–Raphson procedure [34]. This computer program is developed based on nonlinear composite beam theory of Hodges [25] and the finite induced flow model of Peters et al. [31]. NATASHA has been verified and validated with both experimental and numerical benchmarks [6,32,33,36–42].

III. Numerical Simulation

We used three computer programs, Gmsh [43], VABS, and NATASHA; several functions and scripts are developed in MATLAB to connect these software packages and perform the postprocessing of stresses [22,44]. Gmsh has four different modules for creating geometry, mesh, solving, and postprocessing. In this paper, we used only the geometry and mesh modules of this software. The finite element method is used in Gmsh to mesh the cross section of a flying aircraft. We imported these geometries and meshes, with the material properties, into the VABS software to obtain the cross-sectional properties of the fuselage and wings of the aircraft. Next, these properties are used in the computer program NATASHA to perform the stability analysis and provide the trim state results. Finally, these results are returned to the VABS software to acquire the stresses through the wings. Figure 2 presents a schematic view of the numerical simulation procedure in this study.

The design of the aircraft contains two wings with a length of 18 m and a fuselage with a length of 4 m. We used airfoil NACA0012 with a chord of 1 m in this study. Each wing has 18 elements, and the fuselage has four elements. The fuselage is linearly tapered from the center to the root of each wing, and it is treated as a rigid body. There are two engines mounted on the fuselage of the aircraft, in which each engine has a mass equal to 10 kg. This value is constant in all cases that are presented. Nine flaps are considered for each wing, which are distributed between the midspan and the tip of the wings. The schematic view of the designed aircraft is shown in Figs. 3 and 4.

Nine cross-sectional configurations of the wings are displayed in Table 1, and the mechanical properties of these configurations are presented in Tables 2–4. Additionally, Table 5 lists the aerodynamic properties.

IV. Results and Discussion

First, we present the stability of the flying-wing aircraft for all of the nine cases under scrutiny. Next, we analyze the flow of stresses in two separate studies while the total mass in the plane of the cross sections remains identical. In the first study that includes the configurations I–V, we examine the significance of the flow of stresses as we morph the pathways for stresses from the lead-lag direction ($\boldsymbol{b}_2$) to the plunge direction ($\boldsymbol{b}_3$). This study sheds light on the fact that the pathways with thicker branches in the plunge direction improve the aeroelastic stability of the aircraft. In the second case study that includes the configurations V–IX, we focused on improving the flow of stresses in the $\boldsymbol{b}_3$ direction by morphing the pathways of the stresses toward smoother shapes, examining rectangular, triangular, polygonal, circular, and oval configurations.

We investigated the stresses and concluded that the most dominant stresses are $\sigma_{11}, \sigma_{12}, \sigma_{13}$. These findings are in accord with our earlier studies [6,22,44,45]. Therefore, we present σ_{11}, σ_{12}, σ_{13}, and Von Mises stresses in this paper.

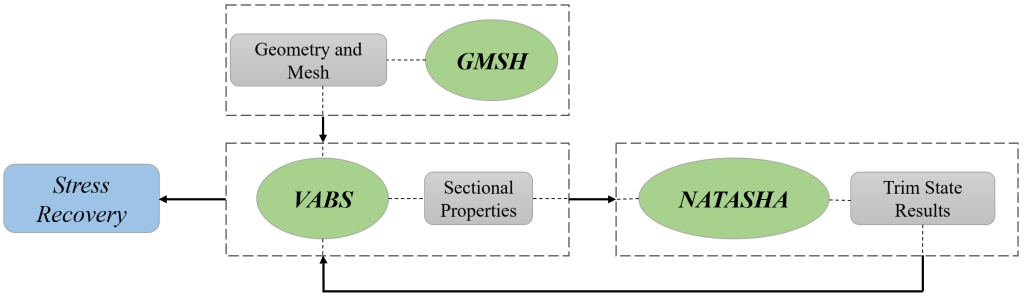

Fig. 2 The simulation procedure.

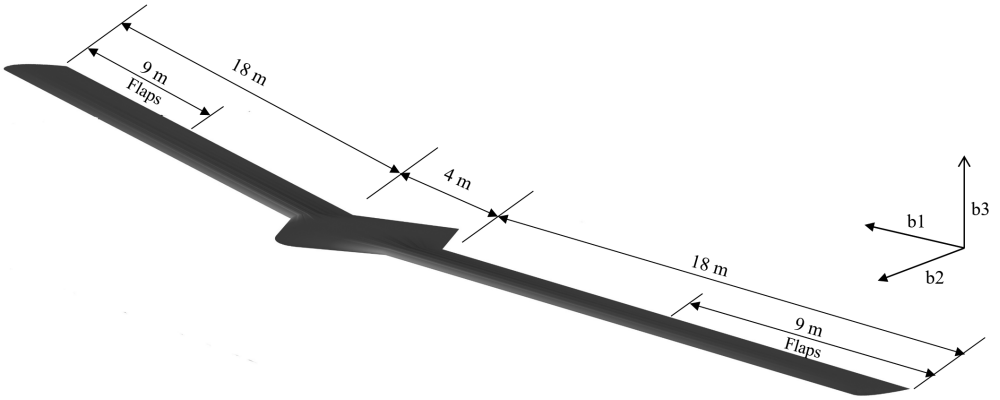

Fig. 3 3-D view of the flying-wing aircraft.

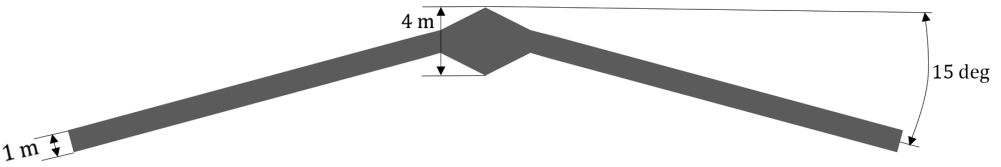

Fig. 4 Top view of the flying-wing aircraft.

Table 1 The configurations of the wing cross sections

Case	Configuration	Case	Configuration	Case	Configuration
I		II		III	
IV		V		VI	
VII		VIII		IX	

Table 2 The cross-sectional properties of the wings for cases I, II, and III in SI unit system

Property	Case I	Case II	Case III
Span, m	20	20	20
R, N^{-1}	$\begin{bmatrix} 3.79\times10^{-9} & 0 & 0 \\ 0 & 1.12\times10^{-8} & 5.33\times10^{-12} \\ 0 & 5.33\times10^{-12} & 6.15\times10^{-7} \end{bmatrix}$	$\begin{bmatrix} 3.80\times10^{-9} & 0 & 0 \\ 0 & 1.20\times10^{-8} & 3.54\times10^{-12} \\ 0 & 3.54\times10^{-12} & 1.20\times10^{-7} \end{bmatrix}$	$\begin{bmatrix} 3.85\times10^{-9} & 0 & 0 \\ 0 & 1.32\times10^{-8} & -1.93\times10^{-13} \\ 0 & -1.93\times10^{-13} & 1.06\times10^{-7} \end{bmatrix}$
S, $N^{-1}\cdot m^{-1}$	$\begin{bmatrix} 0 & -7.10\times10^{-13} & 2.45\times10^{-9} \\ 2.45\times10^{-11} & 0 & 0 \\ -4.10\times10^{-7} & 0 & 0 \end{bmatrix}$	$\begin{bmatrix} 0 & 3.60\times10^{-14} & 2.56\times10^{-9} \\ 2.55\times10^{-13} & 0 & 0 \\ -4.13\times10^{-7} & 0 & 0 \end{bmatrix}$	$\begin{bmatrix} 0 & 1.65\times10^{-13} & 2.96\times10^{-9} \\ -2.31\times10^{-13} & 0 & 0 \\ -4.29\times10^{-7} & 0 & 0 \end{bmatrix}$
T, $N^{-1}\cdot m^{-2}$	$\begin{bmatrix} 3.03\times10^{-6} & 0 & 0 \\ 0 & 5.11\times10^{-6} & -1.67\times10^{-11} \\ 0 & -1.67\times10^{-11} & 5.43\times10^{-8} \end{bmatrix}$	$\begin{bmatrix} 3.552\times10^{-6} & 0 & 0 \\ 0 & 4.892\times10^{-6} & 6.521\times10^{-13} \\ 0 & 6.521\times10^{-13} & 5.464\times10^{-8} \end{bmatrix}$	$\begin{bmatrix} 3.43\times10^{-6} & 0 & 0 \\ 0 & 4.49\times10^{-6} & 2.97\times10^{-12} \\ 0 & 2.97\times10^{-12} & 5.57\times10^{-8} \end{bmatrix}$
I, $kg\cdot m$	$\begin{bmatrix} 3.86\times10^{-1} & 0 & 0 \\ 0 & 3.81\times10^{-3} & 1.11\times10^{-9} \\ 0 & 1.11\times10^{-9} & 3.82\times10^{-1} \end{bmatrix}$	$\begin{bmatrix} 3.86\times10^{-1} & 0 & 0 \\ 0 & 4.10\times10^{-3} & 1.83\times10^{-11} \\ 0 & 1.83\times10^{-11} & 3.82\times10^{-1} \end{bmatrix}$	$\begin{bmatrix} 3.83\times10^{-1} & 0 & 0 \\ 0 & 4.49\times10^{-3} & -1.35\times10^{-12} \\ 0 & -1.35\times10^{-12} & 3.78\times10^{-1} \end{bmatrix}$
ξ, m	$\begin{bmatrix} 0 \\ 5.09\times10^{-2} \\ -2.36\times10^{-18} \end{bmatrix}$	$\begin{bmatrix} 0 \\ 5.26\times10^{-2} \\ -3.23\times10^{-19} \end{bmatrix}$	$\begin{bmatrix} 0 \\ 5.89\times10^{-2} \\ -6.82\times10^{-19} \end{bmatrix}$
Mass, $kg\cdot m^{-1}$	5.513	5.514	5.513
Chord, m	1	1	1

Table 3 Properties of the wings for cases IV, V, and VI in SI units system

Property	Case IV	Case V	Case VI
Span, m	20	20	20
R, N^{-1}	$\begin{bmatrix} 3.90\times10^{-9} & 0 & 0 \\ 0 & 1.50\times10^{-8} & -4.12\times10^{-12} \\ 0 & -4.12\times10^{-12} & 9.50\times10^{-8} \end{bmatrix}$	$\begin{bmatrix} 3.92\times10^{-9} & 0 & 0 \\ 0 & 2.28\times10^{-8} & -3.20\times10^{-12} \\ 0 & -3.20\times10^{-12} & 8.78\times10^{-8} \end{bmatrix}$	$\begin{bmatrix} 3.91\times10^{-9} & 0 & 0 \\ 0 & 1.79\times10^{-8} & -1.20\times10^{-10} \\ 0 & -1.20\times10^{-10} & 9.04\times10^{-8} \end{bmatrix}$
S, $N^{-1}\cdot m^{-1}$	$\begin{bmatrix} 0 & 4.61\times10^{-14} & 3.06\times10^{-9} \\ 1.63\times10^{-11} & 0 & 0 \\ -3.98\times10^{-7} & 0 & 0 \end{bmatrix}$	$\begin{bmatrix} 0 & -3.03\times10^{-14} & 3.28\times10^{-9} \\ 1.78\times10^{-11} & 0 & 0 \\ -4.18\times10^{-7} & 0 & 0 \end{bmatrix}$	$\begin{bmatrix} 0 & -1.23\times10^{-10} & 3.27\times10^{-9} \\ -9.86\times10^{-10} & 0 & 0 \\ -3.99\times10^{-7} & 0 & 0 \end{bmatrix}$
T, $N^{-1}\cdot m^{-2}$	$\begin{bmatrix} 3.29\times10^{-6} & 0 & 0 \\ 0 & 4.18\times10^{-6} & 8.98\times10^{-14} \\ 0 & 8.98\times10^{-14} & 5.69\times10^{-8} \end{bmatrix}$	$\begin{bmatrix} 3.12\times10^{-6} & 0 & 0 \\ 0 & 3.92\times10^{-6} & 1.29\times10^{-12} \\ 0 & 1.29\times10^{-12} & 5.49\times10^{-8} \end{bmatrix}$	$\begin{bmatrix} 3.15\times10^{-6} & 0 & 0 \\ 0 & 3.88\times10^{-6} & 1.38\times10^{-9} \\ 0 & 1.38\times10^{-9} & 5.75\times10^{-8} \end{bmatrix}$
I, $kg\cdot m$	$\begin{bmatrix} 3.78\times10^{-1} & 0 & 0 \\ 0 & 4.82\times10^{-3} & -4.27\times10^{-12} \\ 0 & -6.74\times10^{-13} & 3.73\times10^{-1} \end{bmatrix}$	$\begin{bmatrix} 3.94\times10^{-1} & 0 & 0 \\ 0 & 5.09\times10^{-3} & -6.74\times10^{-13} \\ 0 & -4.27\times10^{-12} & 3.85\times10^{-1} \end{bmatrix}$	$\begin{bmatrix} 3.75\times10^{-1} & 0 & 0 \\ 0 & 5.17\times10^{-3} & -1.48\times10^{-4} \\ 0 & -1.48\times10^{-4} & 3.70\times10^{-1} \end{bmatrix}$
ξ, m	$\begin{bmatrix} 0 \\ 6.31\times10^{-2} \\ -8.48\times10^{-19} \end{bmatrix}$	$\begin{bmatrix} 0 \\ 6.14\times10^{-2} \\ 8.92\times10^{-19} \end{bmatrix}$	$\begin{bmatrix} 0 \\ 6.23\times10^{-2} \\ 5.46\times10^{-5} \end{bmatrix}$
Mass, $kg\cdot m^{-1}$	5.512	5.513	5.514
Chord, m	1	1	1

The flutter speed and frequency of cases I–IX are presented in Fig. 5 and Table 6. These results illustrate that the stability of the flying-wing aircraft increases significantly by changing the configuration of the wing cross section. Cases I–V show that removing the mass from the $\boldsymbol{b}_2$ direction and adding the removed mass to the branches in the $\boldsymbol{b}_3$ direction increases the flutter speed. Furthermore, cases V–IX indicate that shapes such as a rectangle, triangle, polygon, circle, and oval affect the flutter speed of the aircraft significantly. Table 6 shows that the divergence speed increases by changing the wing cross-section configuration from case I to IX. The divergence speed of case IX is approximately 21% greater than case I."

Downloaded by Karina Bustillo on September 13, 2021 | http://arc.aiaa.org | DOI: 10.2514/1.J060410

Table 4 The cross-sectional properties of the wings for cases VII, VIII, and IX in SI unit system

Property	Case VII	Case VIII	Case IX
Span, m	20	20	20
R, N^{-1}	$\begin{bmatrix} 3.86\times10^{-9} & 0 & 0 \\ 0 & 1.90\times10^{-8} & 1.66\times10^{-13} \\ 0 & 1.66\times10^{-13} & 8.46\times10^{-8} \end{bmatrix}$	$\begin{bmatrix} 3.88\times10^{-9} & 0 & 0 \\ 0 & 1.78\times10^{-8} & 3.26\times10^{-12} \\ 0 & 3.26\times10^{-12} & 8.50\times10^{-8} \end{bmatrix}$	$\begin{bmatrix} 3.87\times10^{-9} & 0 & 0 \\ 0 & 1.68\times10^{-8} & 1.96\times10^{-12} \\ 0 & 1.96\times10^{-12} & 8.13\times10^{-8} \end{bmatrix}$
S, $N^{-1}\cdot m^{-1}$	$\begin{bmatrix} 0 & -1.42\times10^{-14} & 2.79\times10^{-9} \\ -7.50\times10^{-13} & 0 & 0 \\ -3.76\times10^{-7} & 0 & 0 \end{bmatrix}$	$\begin{bmatrix} 0 & 2.72\times10^{-14} & 2.97\times10^{-9} \\ -9.44\times10^{-12} & 0 & 0 \\ -3.63\times10^{-7} & 0 & 0 \end{bmatrix}$	$\begin{bmatrix} 0 & 5.04\times10^{-14} & 3.08\times10^{-9} \\ -1.04\times10^{-11} & 0 & 0 \\ -3.47\times10^{-7} & 0 & 0 \end{bmatrix}$
T, $N^{-1}\cdot m^{-2}$	$\begin{bmatrix} 3.00\times10^{-6} & 0 & 0 \\ 0 & 3.73\times10^{-6} & -2.86\times10^{-13} \\ 0 & -2.86\times10^{-13} & 5.58\times10^{-8} \end{bmatrix}$	$\begin{bmatrix} 2.82\times10^{-6} & 0 & 0 \\ 0 & 3.66\times10^{-6} & 1.60\times10^{-13} \\ 0 & 1.60\times10^{-13} & 5.44\times10^{-8} \end{bmatrix}$	$\begin{bmatrix} 2.74\times10^{-6} & 0 & 0 \\ 0 & 3.60\times10^{-6} & 5.24\times10^{-13} \\ 0 & 5.24\times10^{-13} & 5.86\times10^{-8} \end{bmatrix}$
I, kg · m	$\begin{bmatrix} 3.82\times10^{-1} & 0 & 0 \\ 0 & 5.41\times10^{-3} & 1.30\times10^{-13} \\ 0 & 1.30\times10^{-13} & 3.76\times10^{-1} \end{bmatrix}$	$\begin{bmatrix} 3.94\times10^{-1} & 0 & 0 \\ 0 & 5.51\times10^{-3} & -1.25\times10^{-12} \\ 0 & -1.25\times10^{-12} & 3.88\times10^{-1} \end{bmatrix}$	$\begin{bmatrix} 3.66\times10^{-1} & 0 & 0 \\ 0 & 5.60\times10^{-3} & -1.35\times10^{-12} \\ 0 & -1.35\times10^{-12} & 3.60\times10^{-1} \end{bmatrix}$
ξ, m	$\begin{bmatrix} 0 \\ 5.56\times10^{-2} \\ -3.60\times10^{-19} \end{bmatrix}$	$\begin{bmatrix} 0 \\ 6.03\times10^{-2} \\ -1.28\times10^{-18} \end{bmatrix}$	$\begin{bmatrix} 0 \\ 5.80\times10^{-2} \\ 4.27\times10^{-18} \end{bmatrix}$
Mass, $kg\cdot m^{-1}$	5.513	5.513	5.514
Chord, m	1	1	1

Table 5 The aerodynamic properties and coefficients of the wings

Property	e, m	c_{l_α}	c_{l_β}	c_{d_0}	c_{m_0}	c_{m_α}	c_{m_β}	ρ, kg · m^{-3}
Value	0.25	2π	1	0.01	0.0	−0.08	−0.25	0.0889

This study shows that case IX experiences flutter instability at 50.16 m/s with 0.87 Hz, which has the highest flutter speed among the cases. The normalized real and imaginary parts of eigenvalues of this case are presented in Fig. 6. The eigenvalues and speed are normalized with the associated flutter frequency and speed, respectively. This figure presents the coalescence of first bending and short-period modes of the aircraft at the frequency of 0.87 Hz. Figure 7 shows the body-freedom flutter mode of the aircraft for case IX.

The natural mode shapes and frequencies are presented in Table 7. The results demonstrate that the natural frequencies vary by changing the wing cross-section configuration. The frequencies of first and third bending modes increase from case I to IX, whereas the second bending mode frequency slightly decreases from case I to III, and then it increases from case III to IX. The frequencies of torsional modes decrease from case I to II, and then increase from case II to IX.

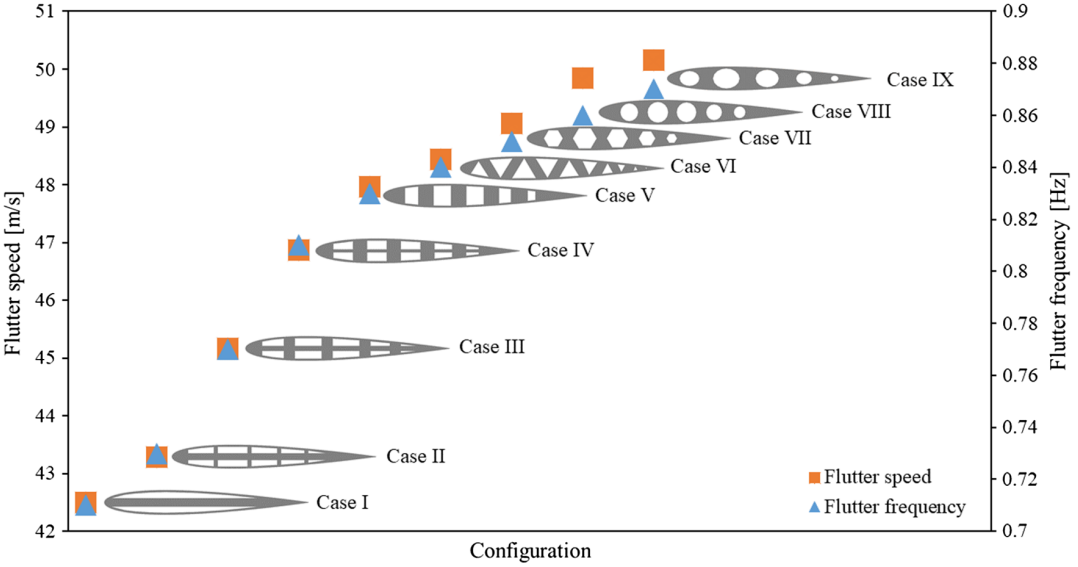

Fig. 5 Flutter characteristics of nine cross-section configurations of a wing.

Table 6 Aeroelastic instability characteristics of nine cross-section configurations of a wing

Case	I	II	III	IV	V	VI	VII	VIII	IX
Flutter speed, m/s	42.50	43.28	45.16	46.87	47.97	48.44	49.06	49.84	50.16
Flutter frequency, Hz	0.71	0.73	0.77	0.81	0.83	0.84	0.85	0.86	0.87
Divergence speed, m/s	66.72	69.37	73.12	76.09	77.97	79.06	79.53	80.62	80.94

Downloaded by Karina Bustillo on September 13, 2021 | http://arc.aiaa.org | DOI: 10.2514/1.J060410

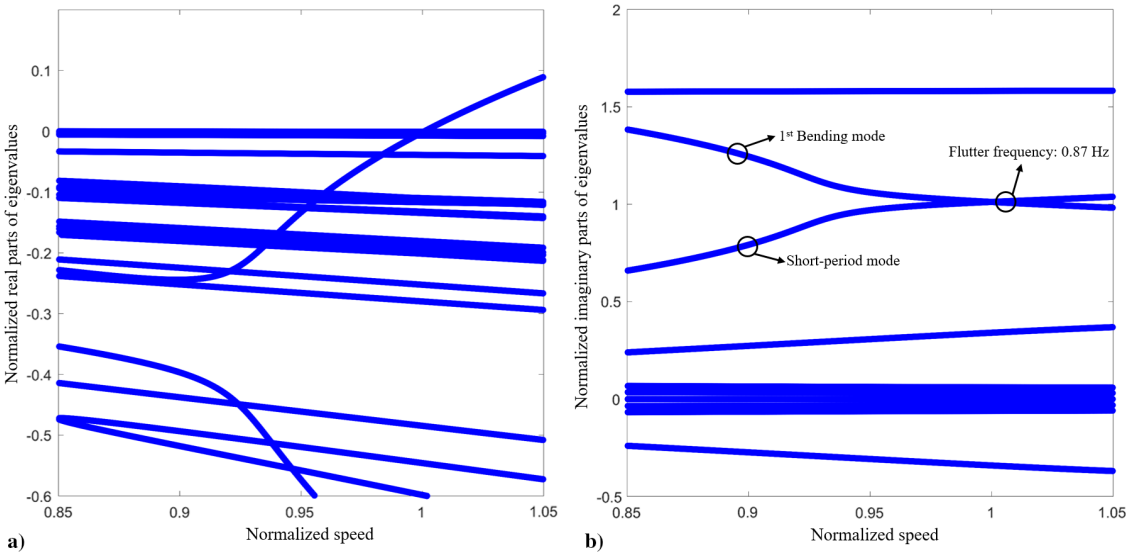

Fig. 6 Eigenvalue behavior of case IX: a) real parts, and b) imaginary parts.

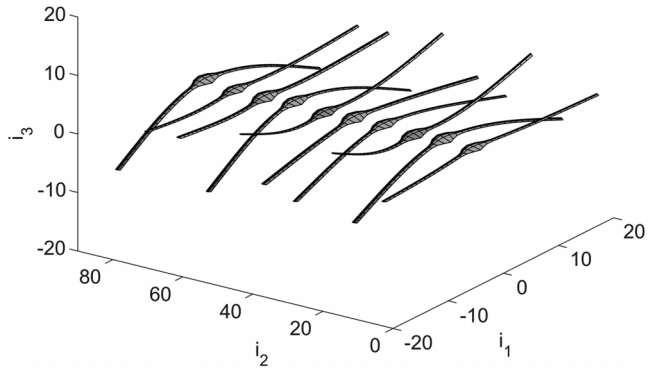

Fig. 7 Body-freedom flutter mode shape of case IX.

The stability analysis demonstrates the advantage of using circular and oval voids in the design of a wing cross section. In the following sections, we present how the stresses flow through the configurations, and we discuss the analogy between instability and stress distributions.

A. Case Study 1

In this section, we study the flow of stresses of the wing cross-section configuration I–V. We derived the flow of stresses for all cases under the same flight condition at the cruise speed of 40 m/s. Case I does not have any branches in the plunge direction ($\boldsymbol{b}_3$). The thickness of the branches in the $\boldsymbol{b}_3$ direction increases from case II to IV. Therefore, the thickness of the strip in the $\boldsymbol{b}_2$ decreases. Case V presents a configuration that only has branches in the $\boldsymbol{b}_3$ direction. We present the flow of stresses for these cases in Figs. 8–11.

Figure 8 shows the distribution of σ_{11}, which indicates that all the configurations are under compression at the upper surface and under tension at the lower surface of the wing. The magnitude of this component of the stress decreases from case I to V. The distribution of σ_{11} becomes smoother when the configuration changes from case I to V. Case V has the highest flutter speed. Our study shows that this case has the smoothest distribution of σ_{11} among the other cases.

Figures 9 and 10 present the σ_{12} and σ_{13} distributions. σ_{13} flows mainly in the stress-carrying pathways, in the $\boldsymbol{b}_2$ direction. As the thickness of the pathway in the $\boldsymbol{b}_2$ direction decreases, stress strangulation occurs; see case V. However, the magnitude of these stresses is significantly smaller than σ_{11}: σ_{12} is one order of magnitude smaller, and σ_{13} is two orders of magnitude smaller than σ_{11}. These findings indicate that σ_{11} plays the major role in affecting the stability of the aircraft.

Figure 11 illustrates the Von Mises stress distribution of case I–V. The strip (i.e., the stress pathway in the $\boldsymbol{b}_2$ direction) does not carry a significant amount of the flow of Von Mises stresses. Hence, the burden of carrying the flow of Von Mises stresses belongs mainly to the skin of the wing profile. The Von Mises stress concentration decreases in the outer region of the cross section from case I to V. Finally, case V has a lower magnitude of Von Mises stress distribution, resulting in higher flutter speed than in the other cases in this section of the study.

This study indicates that stresses flow mainly in the plunge direction ($\boldsymbol{b}_3$) throughout the cross section of the wing, and the strip in the $\boldsymbol{b}_2$ direction does not play a major role in carrying the stresses. Furthermore, smoother flow of stresses and better stability occur in case V, which has wider branches in the $\boldsymbol{b}_3$ direction. Therefore, we focus on improving the stress-carrying pathway configurations that are affective in the $\boldsymbol{b}_3$ direction.

B. Case Study 2

Based on the conclusion reached in the preceding section, here we concentrate on the flow of stresses in the plunge direction $\boldsymbol{b}_3$ through the cross section of the wing. We design the configurations only with

Table 7 Natural mode shape frequencies of nine cross-section configurations of a wing

	Frequency, Hz								
Mode	I	II	III	IV	V	VI	VII	VIII	IX
First bending	1.13	1.36	1.43	1.48	1.52	1.54	1.56	1.58	1.60
Second bending	3.90	3.88	3.85	3.98	4.07	4.13	4.20	4.22	4.30
Third bending	6.91	7.09	7.41	7.68	7.87	7.97	8.11	8.17	8.31
First torsional	12.91	12.09	12.42	12.82	12.93	13.17	13.28	13.53	14.23
Second torsional	39.51	36.55	37.52	38.72	39.10	39.82	40.18	40.92	43.01
Third torsional	66.67	61.51	63.13	65.15	65.71	66.96	67.51	68.80	72.38

Downloaded by Karina Bustillo on September 13, 2021 | http://arc.aiaa.org | DOI: 10.2514/1.J060410

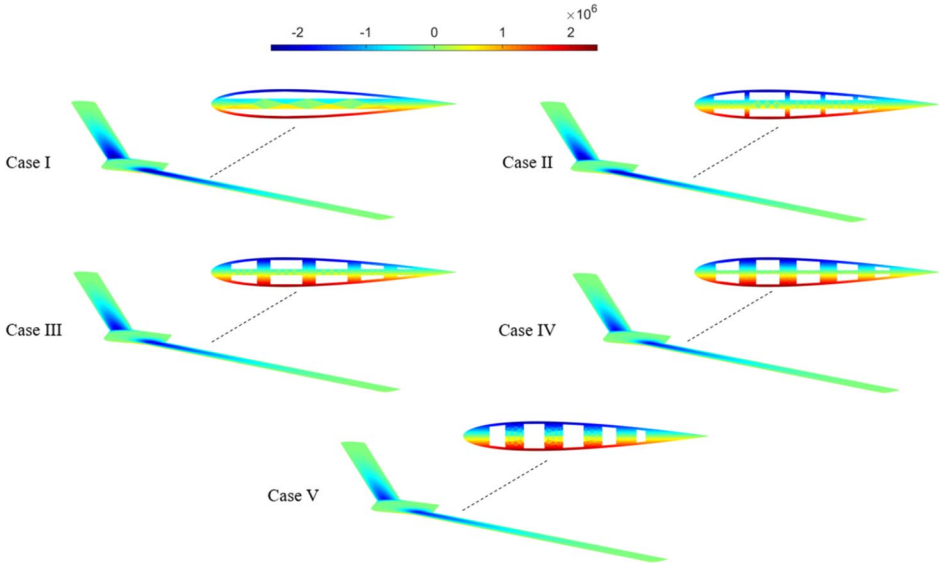

Fig. 8 Study 1, σ_{11} (pa) distribution of wing cross section at the cruise speed of 40 m/s.

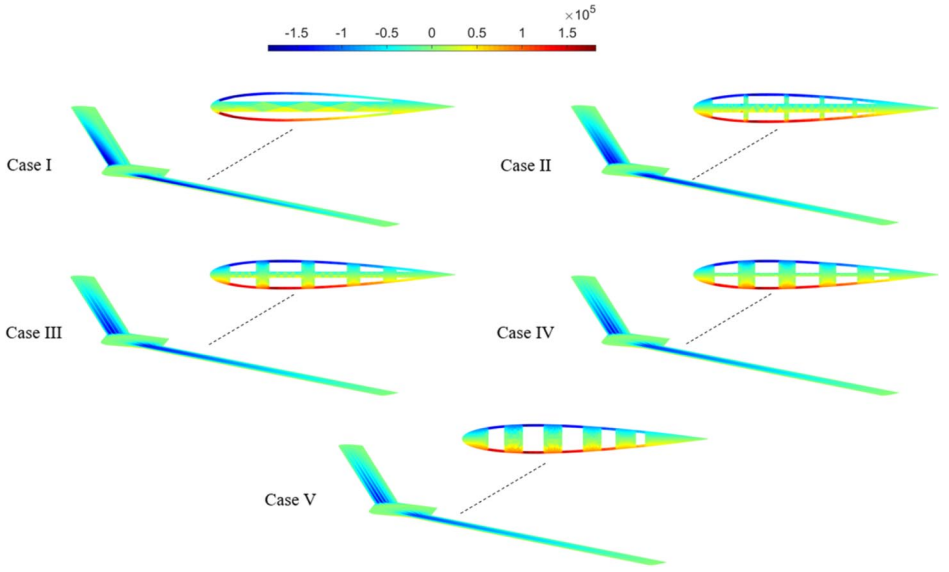

Fig. 9 Study 1, σ_{12} (pa) distribution of wing cross section at the cruise speed of 40 m/s.

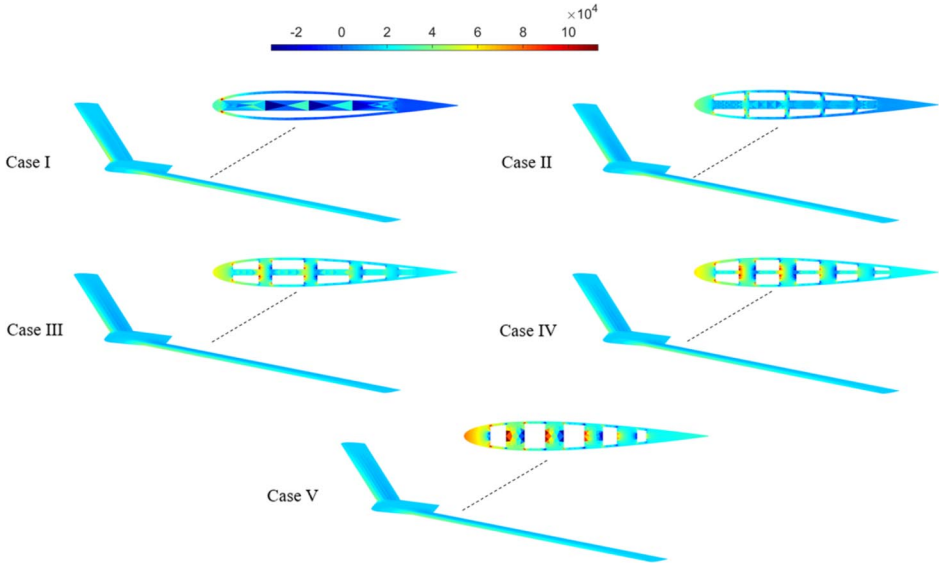

Fig. 10 Study 1, σ_{13} (pa) distribution of wing cross section at the cruise speed of 40 m/s.

Downloaded by Karina Bustillo on September 13, 2021 | http://arc.aiaa.org | DOI: 10.2514/1.J060410

Downloaded by Karina Bustillo on September 13, 2021 | http://arc.aiaa.org | DOI: 10.2514/1.J060410

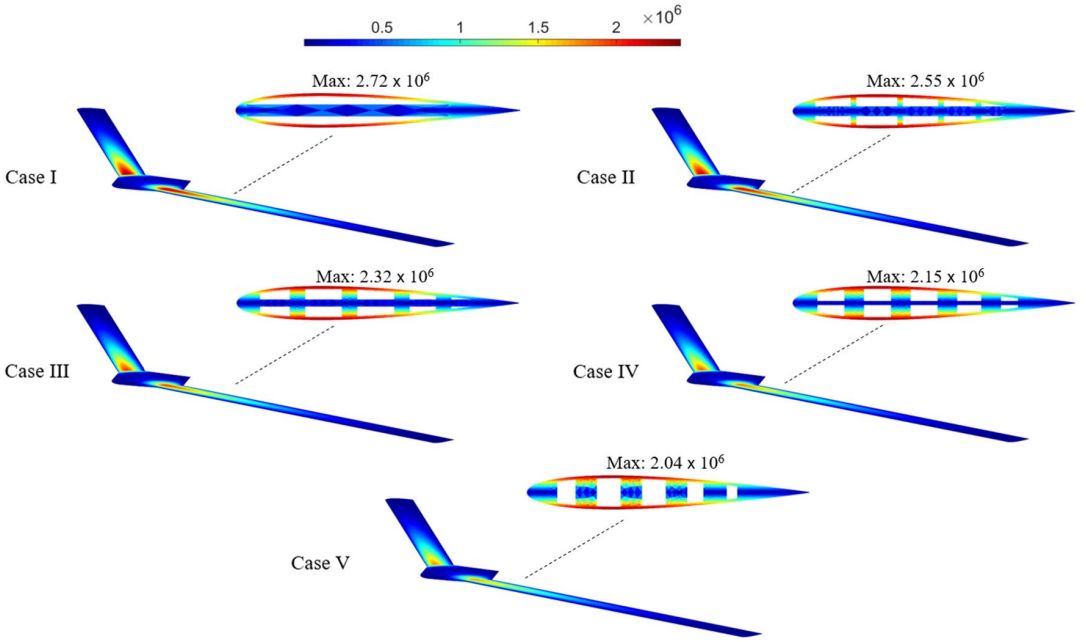

Fig. 11 Study 1, Von Mises stress (pa) distribution of wing cross section at the cruise speed of 40 m/s.

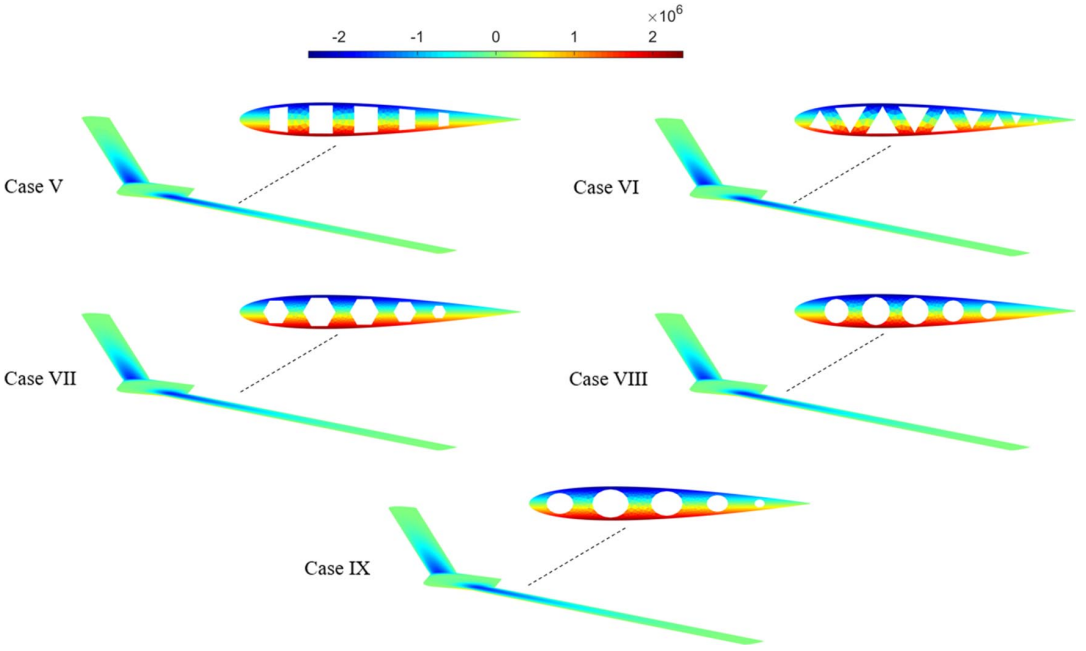

Fig. 12 Study 2, σ_{11} (pa) distribution of wing cross section at the cruise speed of 40 m/s.

branches in the $\boldsymbol{b}_3$ direction, and morph these stress–carrying pathways using shapes, such as a rectangle, triangle, polygon, circle, and oval. Similar to our approach in the preceding section, we maintain the same flight condition (i.e., cruise speed of 40 m/s) and cross-sectional mass distribution. Figures 12–15 present the stress distribution for case V–IX. The distribution of σ_{11} indicates that the upper and lower wing surfaces are under compression and tension, respectively. The magnitude of σ_{11} decreases from case V to IX. Case IX has a smoother flow of stresses compared to the other configurations and has a higher flutter speed.

Figures 13 and 14 show σ_{12} and σ_{13} distributions. Stress strangulation for both σ_{12} and σ_{13} appear in all stress-carrying pathways of the configurations. However, because the magnitude of these stresses are considerably smaller than σ_{11}, their effect on the aeroelastic stability of the aircraft is less significant.

Figure 15 shows the Von Mises stress distribution for case V–IX. Case V is exhibiting significant stress strangulation at the root of the wing. This stress strangulation becomes smoother as we morph the configuration from the rectangular pattern in case V, to the oval pattern in case IX. Case IX has a smoother flow of stresses and achieves higher flutter speed. Noteworthy is that case IX has the smoothest stress distribution and the highest flutter speed among all the configurations in this study.

This section shows that the configurations with curved or smooth edges achieve a smoother flow of stresses, which results in a higher flutter speed than in other configurations.

The stress distribution of σ_{11} for cases with sharp edges, such as a rectangular pattern in case V and triangular pattern in case VI, shows that the stresses accumulate around those edges, the stress strangulations increase, and the flutter speed decreases.

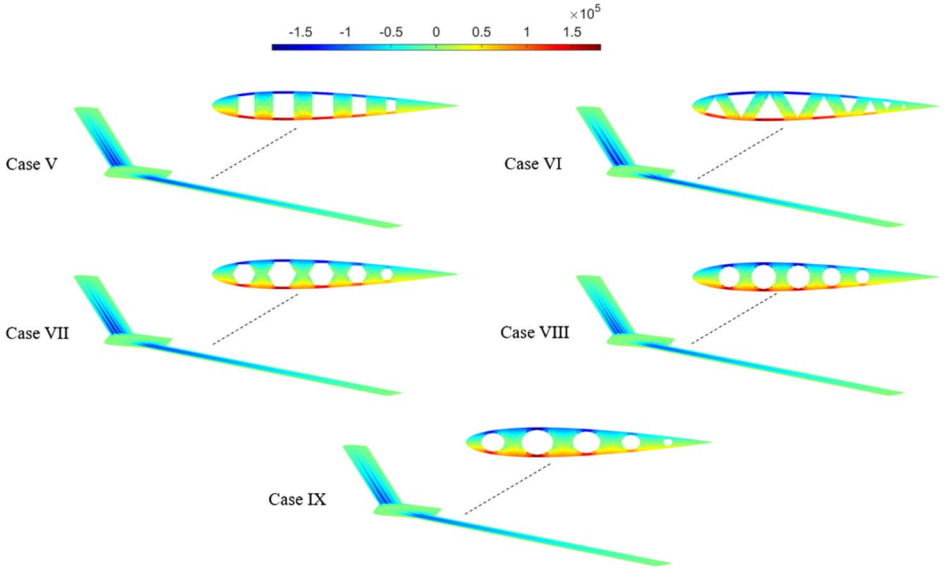

Fig. 13 Study 2, σ_{12} (pa) distribution of wing cross section at the cruise speed of 40 m/s.

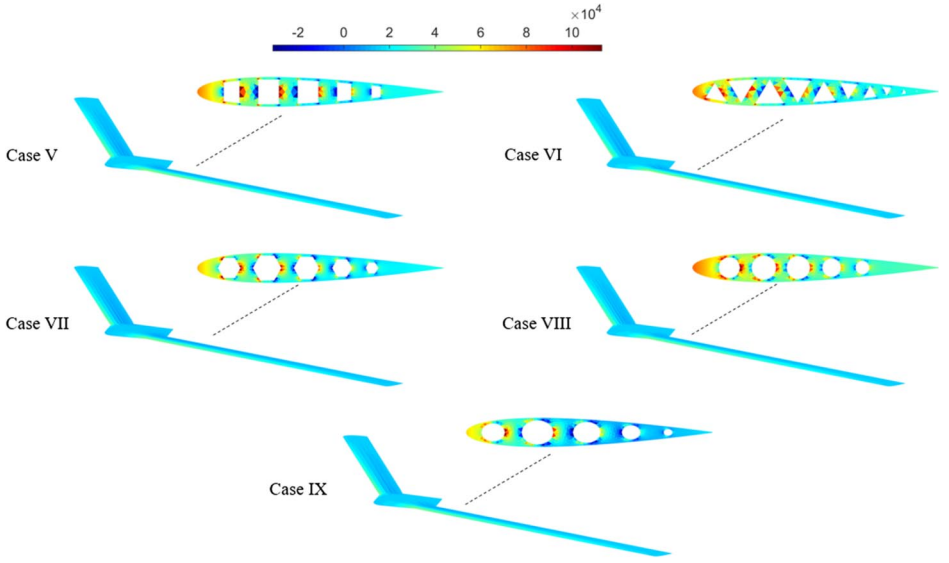

Fig. 14 Study 2, σ_{13} (pa) distribution of wing cross section at the cruise speed of 40 m/s.

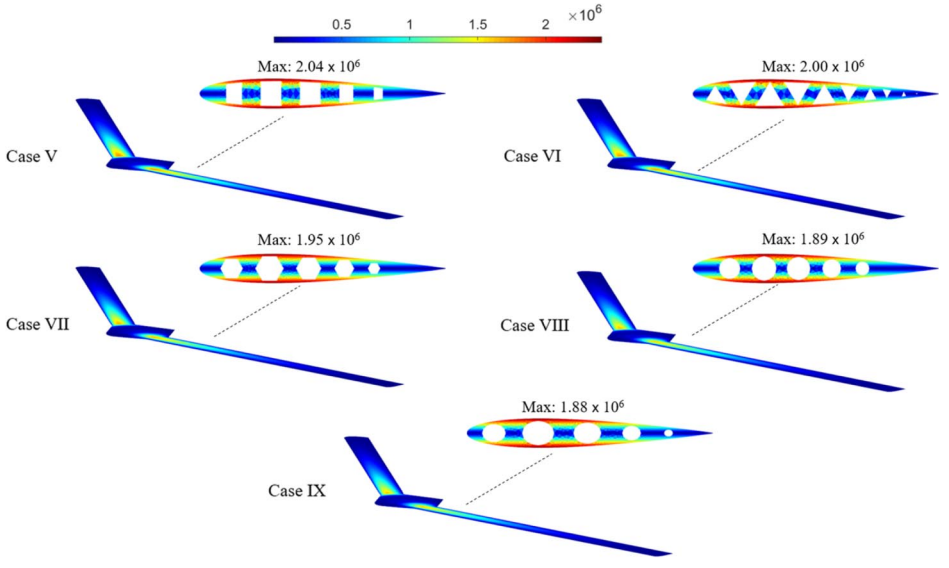

Fig. 15 Study 2, Von Mises stress (pa) distribution of wing cross section at the cruise speed of 40 m/s.

Downloaded by Karina Bustillo on September 13, 2021 | http://arc.aiaa.org | DOI: 10.2514/1.J060410

Downloaded by Karina Bustillo on September 13, 2021 | http://arc.aiaa.org | DOI: 10.2514/1.J060410

V. Conclusions

The configuration of the cross section of the wing significantly affects the aeroelastic stability of a flying-wing aircraft. In this paper, we invoked the constructal law and the concept of the flow of stresses to investigate the aeroelastic stability of nine configurations of the cross sections of the wings of a flying-wing aircraft. The mass per unit length, material, and cruise condition are maintained constant as the configurations of the cross sections of the wings change.

The results show that the magnitude and the flow of stresses change from case I to case IX. This indicates that σ_{11} and Von Mises stresses have a critical role in the analysis and prediction of the aeroelastic instabilities of the aircraft.

The first section of this study compares the significance of the flow of stresses in the stress-carrying pathways in the lead-lag direction ($\boldsymbol{b}_2$) with the stress-carrying pathways in the plunge direction ($\boldsymbol{b}_3$). We remove mass from the strip in the $\boldsymbol{b}_2$ direction and generate branches in the $\boldsymbol{b}_3$ direction while the total cross-sectional mass remains constant. Our results indicate that the branches in the $\boldsymbol{b}_3$ direction are the major stress-carrying pathway compared with the strip in the $\boldsymbol{b}_2$ direction, and play the major role in the flow of stresses affecting the aeroelastic stability of the flying-wing aircraft.

The focus of the second section of our study was to improve the distribution of the flow of stresses and avoid stress strangulations in the configurations where the branching is the dominant pattern. We implemented shapes such as rectangular, triangular, polygonal, circular, and oval to design the cross sections. The results show that the flow of stresses is smoother in the shapes with curved edges, such as circle and oval. Hence, the aeroelastic stability of the aircraft improves. On the other hand, the configurations with sharp edges, such as rectangle or triangle, create stress concentrates in the wing cross section, and the flutter speed drops.

Finally, comparing the stability results shows that the cases with higher flutter speed are associated with the cross-sectional patterns that have the smoothest flow of stresses in the pathways oriented in the plunge direction of the airfoil. The cases with circular and oval voids are among the best designs that accommodate the flow of the stresses smoothly around the curved geometries.

Acknowledgments

The U.S. National Science Foundation (NSF) supports Pezhman Mardanpour's research under grant 1934749.

References

[1] Bejan, A., Charles, J., and Lorente, S., "The Evolution of Airplanes," *Journal of Applied Physics*, Vol. 116, No. 4, 2014, Paper 044901.

[2] Bejan, A., Gunes, U., and Sahin, B., "The Evolution of Air and Maritime Transport," *Applied Physics Reviews*, Vol. 6, No. 2, 2019, Paper 021319.

[3] Chen, R., Wen, C., Lorente, S., and Bejan, A., "The Evolution of Helicopters," *Journal of Applied Physics*, Vol. 120, No. 1, 2016, Paper 014901.

[4] Bejan, A., Gunes, U., Charles, J., and Sahin, B., "The Fastest Animals and Vehicles are Neither the Biggest Nor the Fastest over Lifetime," *Scientific Reports*, Vol. 8, No. 1, 2018, pp. 1–11.

[5] Bejan, A., Charles, J., Lorente, S., and Dowell, E., "Evolution of Airplanes, and What Price Speed?" *AIAA Journal*, Vol. 54, No. 3, 2016, pp. 1120–1123. https://doi.org/10.2514/1.J054481

[6] Mardanpour, P., Izadpanahi, E., Rastkar, S., Lorente, S., and Bejan, A., "Constructal Design of Aircraft: Flow of Stresses and Aeroelastic Stability," *AIAA Journal*, Vol. 57, No. 10, 2019, pp. 4393–4405.

[7] Bejan, A., *Shape and Structure, from Engineering to Nature*, Cambridge Univ. Press, Cambridge, England, U.K., 2000.

[8] Bejan, A., and Lorente, S., *Design with Constructal Theory*, Wiley, Hoboken, NJ, 2008.

[9] Bejan, A., and Lorente, S., "Constructal Law of Design and Evolution: Physics, Biology, Technology, and Society," *Journal of Applied Physics*, Vol. 113, No. 15, 2013, Paper 151301. https://doi.org/10.1063/1.4798429

[10] Rao, J., Kiran, S., Kamesh, J., Padmanabhan, M. A., and Chandra, S., "Topology Optimization of Aircraft Wing," *Journal of Aerospace Science and Technologies*, Vol. 61, No. 3, 2009, p. 402.

[11] Schuhmacher, G., Murra, I., Wang, L., Laxander, A., O'Leary, O., and Herold, M., "Multidisciplinary Design Optimization of a Regional Aircraft Wing Box," *9th AIAA/ISSMO Symposium on Multidisciplinary Analysis and Optimization*, AIAA Paper 2002-5406, 2002.

[12] Zhu, J.-H., Zhang, W.-H., and Xia, L., "Topology Optimization in Aircraft and Aerospace Structures Design," *Archives of Computational Methods in Engineering*, Vol. 23, No. 4, 2016, pp. 595–622.

[13] Oktay, E., Akay, H., and Merttopcuoglu, O., "Parallelized Structural Topology Optimization and CFD Coupling for Design of Aircraft Wing Structures," *Computers and Fluids*, Vol. 49, No. 1, 2011, pp. 141–145.

[14] Hanif, A., Li, H., Raza, M., Kamran, M., and Abdullah, M., "Optimization Design of an Aircraft Wing Structure Based on Response Surface Method," *IOP Conference Series: Materials Science and Engineering*, Vol. 887, IOP Publ., Bristol, U.K., 2020, Paper 012024.

[15] Kim, K.-T., "Free Vibration of Composite Thin-Walled Beams with Chordwise Asymmetric Closed Cross-Sections," *International Journal of Aerospace Engineering*, Vol. 2019, Feb. 2019, pp. 1–14.

[16] Farsadi, T., and Hasbestan, J., "Calculation of Flutter and Dynamic Behavior of Advanced Composite Swept Wings with Tapered Cross Section in Unsteady Incompressible Flow," *Mechanics of Advanced Materials and Structures*, Vol. 26, No. 4, 2019, pp. 314–332.

[17] Tang, J., Xi, P., Zhang, B., and Hu, B., "A Finite Element Parametric Modeling Technique of Aircraft Wing Structures," *Chinese Journal of Aeronautics*, Vol. 26, No. 5, 2013, pp. 1202–1210.

[18] Librescu, L., and Song, O., "On the Static Aeroelastic Tailoring of Composite Aircraft Swept Wings Modelled as Thin-Walled Beam Structures," *Composites Engineering*, Vol. 2, Nos. 5–7, 1992, pp. 497–512.

[19] Qin, Z., and Librescu, L., "Static and Dynamic Validations of a Refined Thin-Walled Composite Beam Model," *AIAA Journal*, Vol. 39, No. 12, 2001, pp. 2422–2424.

[20] Bejan, A., Lorente, S., and Lee, J., "Unifying Constructal Theory of Tree Roots, Canopies and Forests," *Journal of Theoretical Biology*, Vol. 254, No. 3, 2008, pp. 529–540.

[21] Lorente, S., Lee, J., and Bejan, A., "The "Flow of Stresses" Concept: The Analogy Between Mechanical Strength and Heat Convection," *International Journal of Heat and Mass Transfer*, Vol. 53, Nos. 15–16, 2010, pp. 2963–2968.

[22] Izadpanahi, E., Rastkar, S., and Mardanpour, P., "Constructal Design of Flying Wing Aircraft: Curved and Swept Configurations," *AIAA Journal*, Vol. 57, No. 12, 2019, pp. 5527–5542.

[23] *Pilot's Handbook of Aeronautical Knowledge*, U.S. Dept. of Transportation, Federal Aviation Administration, Airman Testing Standards Branch, Oklahoma City, 2009, Chap. 3.

[24] Kim, S., Lorente, S., and Bejan, A., "Dendritic Vascularization for Countering Intense Heating from the Side," *International Journal of Heat and Mass Transfer*, Vol. 51, Nos. 25–26, 2008, pp. 5877–5886.

[25] Hodges, D. H., "Geometrically Exact, Intrinsic Theory for Dynamics of Curved and Twisted Anisotropic Beams," *AIAA Journal*, Vol. 41, No. 6, 2003, pp. 1131–1137. https://doi.org/10.2514/2.2054

[26] Hodges, D. H., *Nonlinear Composite Beam Theory*, AIAA, Reston, VA, 2006.

[27] Yu, W., Hodges, D. H., and Ho, J. C., "Variational Asymptotic Beam Sectional Analysis—An Updated Version," *International Journal of Engineering Science*, Vol. 59, Oct. 2012, pp. 40–64.

[28] Berdichevskii, V., "Variational-Asymptotic Method of Constructing a Theory of Shells: PMM," *Journal of Applied Mathematics and Mechanics*, Vol. 43, No. 4, 1979, pp. 711–736.

[29] Yu, W., Volovoi, V. V., Hodges, D. H., and Hong, X., "Validation of the Variational Asymptotic Beam Sectional Analysis," *AIAA Journal*, Vol. 40, No. 10, 2002, pp. 2105–2112.

[30] Yu, W., and Hodges, D. H., "Generalized Timoshenko Theory of the Variational Asymptotic Beam Sectional Analysis," *Journal of the American Helicopter Society*, Vol. 50, No. 1, 2005, pp. 46–55.

[31] Peters, D. A., Karunamoorthy, S., and Cao, W.-M., "Finite State Induced Flow Models. I—Two-Dimensional Thin Airfoil," *Journal of Aircraft*, Vol. 32, No. 2, 1995, pp. 313–322. https://doi.org/10.2514/3.46718

[32] Sotoudeh, Z., Hodges, D. H., and Chang, C.-S., "Validation Studies for Aeroelastic Trim and Stability of Highly Flexible Aircraft," *Journal of Aircraft*, Vol. 47, No. 4, 2010, pp. 1240–1247. https://doi.org/10.2514/1.46974

[33] Goland, M., and Luke, Y., "The Flutter of a Uniform Wing with Tip Weights," *Journal of Applied Mechanics*, Vol. 15, No. 1, 1948, pp. 13–20.

[34] Patil, M. J., and Hodges, D. H., "Flight Dynamics of Highly Flexible Flying Wings," *Journal of Aircraft*, Vol. 43, No. 6, 2006, pp. 1790–1799. https://doi.org/10.2514/1.17640

[35] Chang, C.-S., Hodges, D. H., and Patil, M. J., "Flight Dynamics of Highly Flexible Aircraft," *Journal of Aircraft*, Vol. 45, No. 2, 2008, pp. 538–545. https://doi.org/10.2514/1.30890

[36] Timoshenko, S. P., and Gere, J. M., *Theory of Elastic Stability*, 2nd ed., McGraw–Hill, New York, 1961, p. 88.

[37] Simitses, G. J., and Hodges, D. H., *Fundamentals of Structural Stability*, Butterworth-Heinemann, Burlington, 2006, pp. 265, 306.

[38] Dowell, E., Traybar, J., and Hodges, D. H., "An Experimental-Theoretical Correlation Study of Non-Linear Bending and Torsion Deformations of a Cantilever Beam," *Journal of Sound and Vibration*, Vol. 50, No. 4, 1977, pp. 533–544. https://doi.org/10.1016/0022-460X(77)90501-6

[39] Bauchau, O. A., and Kang, N., "A Multibody Formulation for Helicopter Structural Dynamic Analysis," *Journal of the American Helicopter Society*, Vol. 38, No. 2, 1993, pp. 3–14. https://doi.org/10.4050/JAHS.38.3

[40] Bauchau, O. A., "Computational Schemes for Flexible, Nonlinear Multi-Body Systems," *Multibody System Dynamics*, Vol. 2, No. 2, 1998, pp. 169–225. https://doi.org/10.1023/A:1009771081

[41] Saberi, H., Khoshlahjeh, M., Ormiston, R., and Rutkowski, M., "Overview of RCAS and Application to Advanced Rotorcraft Problems," *Proceedings of the American Helicopter Society 4th Decennial Specialists' Conference on Aeromechanics*, San Francisco, CA, Jan. 2004.

[42] Mardanpour, P., Hodges, D. H., Neuhart, R., and Graybeal, N., "Engine Placement Effect on Nonlinear Trim and Stability of Flying Wing Aircraft," *Journal of Aircraft*, Vol. 50, No. 6, 2013, pp. 1716–1725. https://doi.org/10.2514/1.C031955

[43] Geuzaine, C., and Remacle, J.-F., "Gmsh: A 3-D Finite Element Mesh Generator with Built-in Pre- and Post-Processing Facilities," *International Journal for Numerical Methods in Engineering*, Vol. 79, No. 11, 2009, pp. 1309–1331.

[44] Izadpanahi, E., Moshtaghzadeh, M., Radnezhad, H. R., and Mardanpour, P., "Constructal Approach to Design of Wing Cross-Section for Better Flow of Stresses," *AIAA Scitech 2020 Forum*, AIAA Paper 2020-0275, 2020.

[45] Mardanpour, P., Izadpanahi, E., Powell, S., Rastkar, S., and Bejan, A., "Inflected Wings in Flight: Uniform Flow of Stresses Makes Strong and Light Wings for Stable Flight," *Journal of Theoretical Biology*, Vol. 508, Jan. 2021, Paper 110452.

D. E. Raveh
Associate Editor

Downloaded by Karina Bustillo on September 13, 2021 | http://arc.aiaa.org | DOI: 10.2514/1.J060410